Efficient Aero-Acoustic Simulation of the HART II Rotor with the Compact Pade Scheme

Gunther Wilke
Institute of Aerodynamics and Flow Technolgy
German Aerospace Center (DLR) Braunschweig
Lilienthalplatz 7, 38106 Braunschweig, Germany

Abstract

One major difficulty in the design of quiet rotor blades is the correct numerical prediction of blade vortex interaction (BVI) noise in descent flight. Current second order spatial discretization schemes inherently have too much numerical dissipation to correctly conserve vorticity in the computational fluid dynamics (CFD) simulation. Higher order methods have proven their worthiness to alleviate this problem, yet are costly in terms of computational resources. In this paper, the 4^{th} order implicit compact Pade scheme based on the finite difference formulation of the RANS equations is employed to convect the vortices in the simulation. The approach is paired with the classical finite volume approach with the Jameson-Schmidt-Turkel (JST) scheme. The robustness and flexibility of the JST scheme are exploited in the near field of the rotor blades and fuselage, while in the mid- and farfield the Pade scheme is utilized. This approach is validated against the experimental data of the HART II wind tunnel campaign. Different grid resolutions are examined as well as simulation strategies ranging from inviscid isolated rotor simulation up to viscous simulation including the fuselage. This hybrid simulation technique demonstrates the usefulness due to its high efficiency, while for design purposes the simplified physics yield an additional speed-up of the turn-around time.

1 INTRODUCTION

Helicopters are noisy in their operation. Especially in the descent flight condition upon the landing approach, a slapping of the rotor is heard. This phenomenon is known as blade-vortex interaction (BVI) noise. The tip vortices that trail off the blades are hit again by the following blades. In particular when these vortices are parallel to the passing blade, a fast change of angle-of-attack occurs on the blade leading to sudden changes in the airloads on the blade. This effect causes most of the noise generated in the descent flight condition, which is also considered during certification. The helicopter must stay under specified noise limits during the approach. Therefore it is highly beneficial for aircraft manufactures to properly predict the rotor noise before it is built.

There is much ongoing research concerning the simulation of BVI noise. The popular test campaign HART-II [1] investigates a scaled BO-105 rotor model in detail in various flight conditions including the BVI dominant descent flight. The purpose of this campaign is to analyze the effect of higher-harmonic controls (HHC) of the rotor blades onto BVI noise. The HART-II test campaign is well documented and therefore creates a good basis for simulation code validation. Smith et al. [2] compare various computational fluid-structural dynamics codes against the experimental HART-II data. Their observation is that the spatial and temporal accuracy of the simulation is crucial for the successful simulation of BVI noise. They state that second order spatial accuracy is insufficient on typical engineering meshes and this is either alleviated by increasing the grid density in regions of interest through mesh adaptation or spatial schemes of higher order accuracy. Recent works by Lim et al. [3] demonstrate that grid refinement greatly contributes to the correct vorticity prediction. Jain et al. [4] proof that a 5^{th} order spatial scheme also enhances the vorticity prediction. Tanabe and Sugawara [5] implement a higher order upwind scheme and demonstrate that it is well suited for vortex conservation. All these works have one thing in common; they split the computational domain into zones with different solution strategies. They compute the near-body grids with a second order finite volume method and apply a higher order scheme in the farfield, which may even be temporally decoupled.

A different approach is gone by Kowarsch et al. [6] for the simulation of BVI noise. They apply the 5^{th} order WENO scheme in the whole computational domain, which is robust but also costly since the WENO scheme evaluates multiple stencils for one cell to combine them in the most optimal way.

The motivation of this work is to try out a new efficient higher-order scheme for the simulation of the HART-II test case. The scheme is a compact implicit higher-order finite difference scheme, the Pade scheme developed by Lele [7]. Due to its implicit nature it is solved quickly in contrast to other schemes. It is also utilized in a zonal approach, where the rotor blades are still modeled with the second order finite-volume scheme by James-Schmidt-Turkel (JST) [8] referred to as a Hybrid simulation or scheme in this paper.

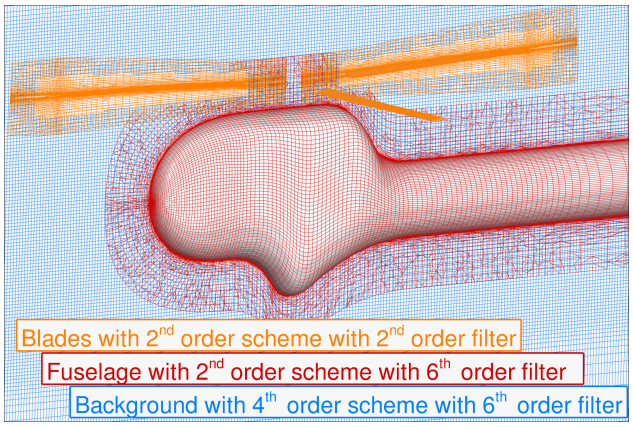

Figure 1: *Schematic of the employment of different numerical schemes.*

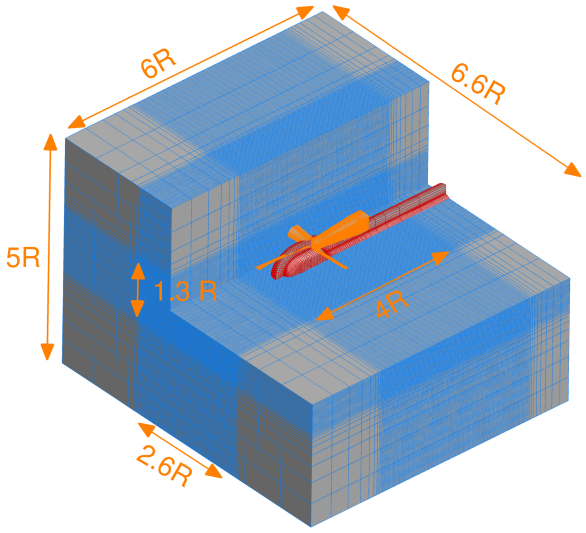

Figure 2: *Schematic of background mesh and its dimensions*

2 METHODOLOGY

For the complete and correct simulation of the helicopter, the blade aero-mechanics need to be solved including the disciplines of aero-, structural- and flight dynamics. Therefore, the simulation of the HART II test case consists of the application of the comprehensive code HOST [9] developed by Airbus Helicopters France to account for the structural- and flight dynamics and the block-structured flow solver FLOWer [10] developed by DLR for the aerodynamics. They are coupled together through the delta airloads approach as validated for FLOWer and HOST by Dietz et al. [11]. The fluid-structural coupling is iterated until less than 0.1% residual change is observed in the required rotor power.

2.1 CFD Strategy

The block-structured solver FLOWer allows the computation of different numerical schemes on different blocks in the computational domains. This is exploited for the sake of stability in the simulation and sketched in Figure 1. The individual regions are marked with different colors. The rotor blades are computed with the 2^{nd} order JST scheme, while the fuselage is computed with a mixed version of JST and Pade scheme, where the flux calculation is based on JST and the numerical dampening is based on a 6^{th} order Pade filter. The background mesh is purely computed with the 4^{th} order Pade Scheme also applying the 6th order Pade filter.

For the following investigation, three types of simulations are setup:

- Inviscid Euler simulation of an isolated rotor (inviscid)
- Viscous Reynolds-Average Navier-Stokes (RANS) simulation of an isolated rotor (viscous)
- Viscous RANS simulation of the rotor with the fuselage (+ fuselage)

The viscous simulations employ the Wilcox $k-\omega$ turbulence model [12] for the calculation of the turbulent viscosity. The reason for these three setups is to determine how much detail is required in the simulation to capture the noise signature of the BVI dominant descent flight.

The time is advanced with a 2^{nd} order dual-time stepping scheme, where the inner iterations are computed with a five-stage Runge-Kutta scheme. For the blade and fuselage grids, three levels of multigrid accelerate the convergence, while additionally the Runge-Kutta scheme is implicitly smoothed. The corresponding Courant-Friedrichs-Lewy (CFL) number is chosen to be 7.5.

2.2 Discretization

The frequency range of BVI noise is roughly between 6-40 blade passing frequencies (BPF). This means that a frequency of roughly $1400Hz$ has to be resolved for the upper limit. Using the speed of sound, this yields a minimum wave length of $0.246m$. Assuming the occurring signals are resolved with 10 discretization points, a time step of $3.6 \cdot 10^{-5}s$ is required and a grid spacing of $0.0123m$. This corresponds to a time step equivalent of $\Delta\psi = 0.23^o$ and 10% chord lengths in spacing.

While the time step has an effect on the overall simulation, the grid spacing is most critical for the design of the background mesh. The background mesh is created using an equidistant spacing near the rotor disc and the rotor wake and grows exponentially towards

level	coarse	medium	fine
blade	40,392	323,136	2,585,088
fuselage	61,440	491,520	3,932,160
background	1,382,400	11,059,200	88,473,600
total	1,605,408	12,843,264	102,746,112

Table 1: *Grid sizes at different (multigrid-)levels*

the farfield. Thus, about half the points of the background mesh are in the inner domain, the other half grows towards the farfield. A sketch of the inner and outer part of the background mesh along with its dimensions is shown in Figure 2.

The blade grid generation is done with an in-house grid generator based on the principles of GEROS [13] and enhanced for boundary layer treatment as well as multi-block structures. The inviscid mesh topology is of the type O-H, while the viscous meshes are of the C-H type. For the inviscid meshes, the root, tip and tab of the blade are modified. Instead of utilizing the airfoil of the HART II test campaign, which is a modified NACA23012, the original version of the NACA23012 being closed at the trailing edge is utilized. The blade tip and root are tapered and therefore not blunt as the wind tunnel model. The RANS meshes resemble the wind tunnel geometry closely. The criterion of $y+ = 1$ for the finest grid spacing in the wall normal direction is fulfilled throughout the surface, with the exception that the blade root and tip go beyond $y+ = 1$ to not overly increase the number of required grid points. Both blade tip treatments, inviscid and viscous are visually compared in Figure 3 and their individual topologies in Figure 4.

Three levels of refinement are investigated, see Table 1, which are coarse, medium and fine. The coarse and medium levels are generated from the finest level by leaving out every other grid point in each spatial direction. The distribution of points is listed in Table 2 for the finest level. Accompanying the spatial resolution, the temporal resolution is additionally increased, which is listed in Table 3.

The initial four revolutions correspond to the time required for the rotor wake to leave the computational domain, while the consecutive two revolutions are estimated by $N_{revolutions} = 1/\mu\pi$. The formula reflects the time in number of rotor revolutions a particle needs when it is released at the front of the rotor disc to leave at the aft of the disc in dependency of the advance ratio μ. For the prescribed motion test cases, only the four initial revolutions are performed, which grants a periodic signal, while for the fluid-structural coupled cases an additional two revolutions are run each coupling step until aero-elastic convergence is reached.

2.3 Jameson-Schmidt-Turkel Scheme

For the blade grids, the James-Schmidt-Turkel (JST) [8] scheme is utilized for the spatial representation of the fluxes of the Navier-Stokes equations. The scheme is based on the volume formulation and shows a very robust behavior. The discrete form of JST is stated as:

$$(1)\quad \frac{d}{dt}\vec{W}_{i,j,j}\cdot V_{i,j,k}+\vec{Q}_{i,j,k}+\vec{G}_{i,j,k}\cdot V_{i,j,k}-\vec{D}_{i,j,k}=0$$

with $\vec{W}$ the conservative variables, V the volume, $\vec{Q}$ the surface integral over the fluxes, $\vec{G}$ the source terms for the rotating frame and $\vec{D}$ a numerical dissipation operator at the index location i, j, k. The flux integral $\vec{Q}$ is approximated by the six face of the hexaedric control volume:

$$(2)\qquad \vec{Q}_{i,j,k}=\sum_{s}^{6}(\bar{\bar{F}}_t-\vec{W}_t\cdot\vec{q}_{b_t})\cdot\vec{S}_s$$

with $\bar{\bar{F}}$ the flux density tensor, $\vec{q}_{b_t}$ the motion of the grid cell and $\vec{S}_s$ the surface normal vector. The index t is to be replaced by $i\pm\frac{1}{2}, j, k$ for $t = 1, 2$, $i, j\pm\frac{1}{2}, k$ for $t = 3, 4$, and $i, j, k\pm\frac{1}{2}$ for $t = 5, 6$. The half index $\pm\frac{1}{2}$ denotes the flux averaging which is done to evaluate the value of two cells at the intersecting cell face. The flux density is therefore computed by

$$(3)\qquad \bar{\bar{F}}_{i-\frac{1}{2},j,k}=\bar{\bar{F}}(\vec{W}_{i-\frac{1}{2},j,k})$$

with

$$(4)\qquad \vec{W}_{i-\frac{1}{2},j,k}=\frac{1}{2}(\vec{W}_{i-1,j,k}+\vec{W}_{i,j,k}).$$

This alone yields a formally second order accurate scheme. However, it is not stable over discontinuities by itself and therefore JST implemented the numerical dissipation operator $\vec{D}$, which is similarly evaluated as the surface integral:

$$(5)\qquad \vec{D}_{i,j,k}=\sum_{t}^{3}(\vec{d}_{t+\frac{1}{2}}-d_{t-\frac{1}{2}})$$

with t again the interchanging offset of i, j, k. The dissipative flux $d_{i+\frac{1}{2},j,k}$ is calculated by:

$$(6)\qquad \begin{aligned} d_{i+\frac{1}{2},j,k} &= \epsilon^{(2)}_{i+\frac{1}{2},j,k}(\vec{W}_{i+\frac{1}{2},j,k}-\vec{W}_{i,j,k}) \\ -\epsilon^{(4)}_{i+\frac{1}{2},j,k}&(\vec{W}_{i+2,j,k}-3\vec{W}_{i+1,j,k}+3\vec{W}_{i,j,k}-\vec{W}_{i-1,j,k}) \end{aligned}$$

The coefficients $\epsilon^{(2)}_{i+\frac{1}{2},j,k}$ for strong gradients and $\epsilon^{(4)}_{i+\frac{1}{2},j,k}$ for high-frequency oscillations are computed by:

$$(7)\qquad \epsilon^{(2)}_{i+\frac{1}{2},j,k} = k^{(2)}max(\nu_{i,j,k},\nu_{i+1,j,k})$$

$$(8)\qquad \epsilon^{(4)}_{i+\frac{1}{2},j,k} = max(0,k^{(4)}-\epsilon^{(2)}_{i+\frac{1}{2},j,k})$$

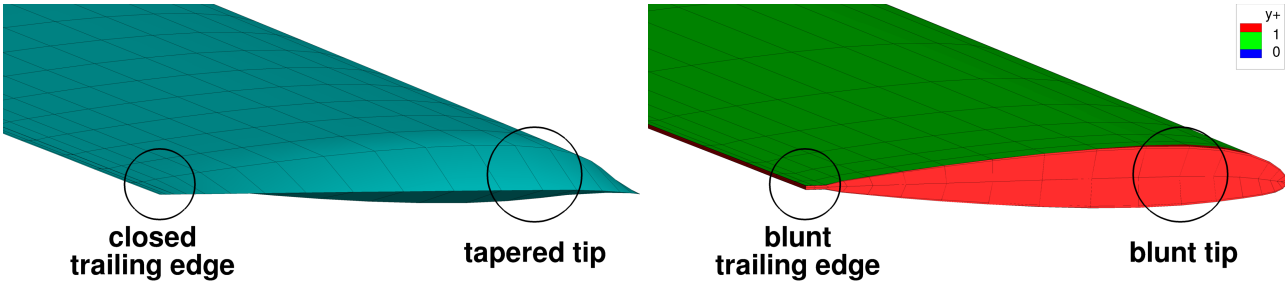

(a) Euler Mesh (b) RANS Mesh

Figure 3: *The blade tips and tabs shown for the different discretizations (coarsest grid level)*

mesh	**inviscid**			**viscous**		
blade	chordwise	radial	normal	chordwise	radial	normal
	161	24+73+48	65	145 + 2 x 41	24+73+48	73
	= 2,211,840 cells			**= 2,585,088 cells**		
fuselage				lengthwise	radial	normal
				257	241	65
				= 3,932,160 cells		
background	inflight		lateral		vertical	
(inner)	554		422		210	
(total)	641		481		289	
	=88,473,600 cells					
total	**= 97,320,960 cells**			= **98,813,952 cells** without fuselage = **102,746,112 cells** with fuselage		

Table 2: *Discretization of the blade for the individual solution strategies at the finest level*

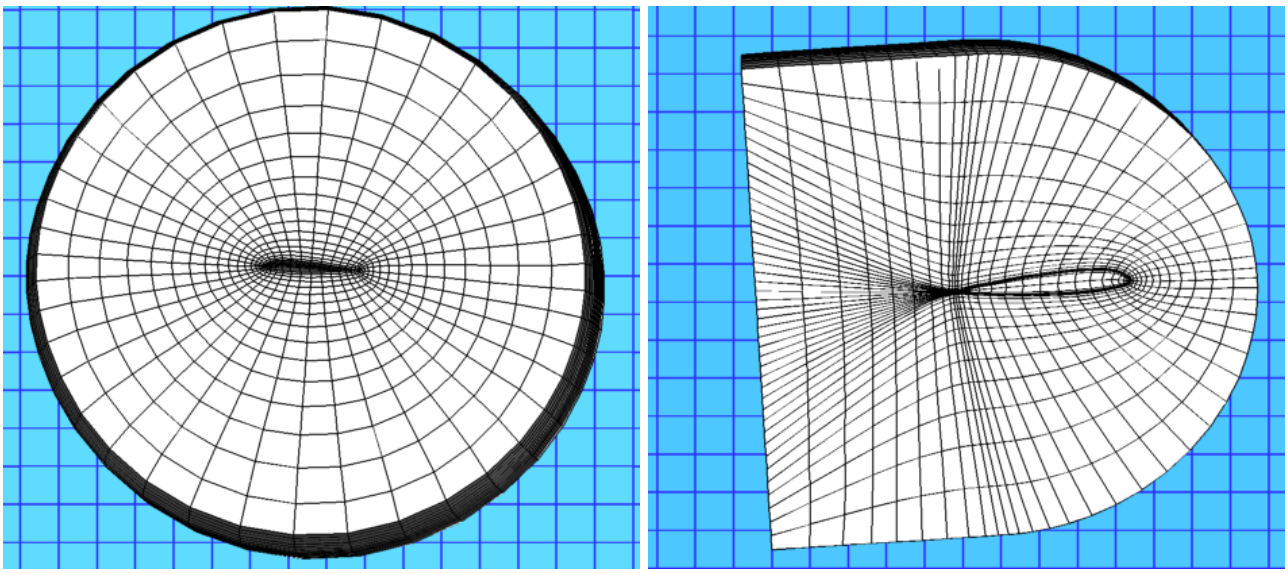

(a) Euler Mesh (b) RANS Mesh

Figure 4: *Blade topologies shown with the inner background mesh spacing for the coarse mesh setups*

with the pressure sensor

$$\nu_{i,j,k} = \left| \frac{p_{i-1,j,k} - 2p_{i,j,k} + p_{i+1,j,k}}{p_{i-1,j,k} + 2p_{i,j,k} + p_{i+1,j,k}} \right|. \quad (9)$$

and $p_{i,j,k}$ the pressure in cell i,j,k. The coefficents $k^{(2)}$ and $k^{(4)}$ are chosen to be $\frac{1}{2}$ and $\frac{1}{128}$ in this work.

2.4 Compact Pade Scheme

The concept of the Pade scheme is to solve the Navier-Stokes equations on a equidistant, Cartesian mesh. As this is not necessarily the case (the background mesh only partially fulfills this condition), a coordinate transformation from a curvilinear grid to the Cartesian grid is necessary. The Navier-Stokes equations in the transformed finite-difference formulation read:

$$\frac{d}{dt}\frac{\vec{W}}{J} + \sum_{i=1}^{3} \frac{\partial \hat{F}_i}{\partial \xi_i} + \frac{\hat{\vec{G}}}{J} = 0 \quad (10)$$

The flux density tensor is now altered $\hat{F}$ and built with the contravariant velocity $\hat{U}$:

$$\hat{F}_i = \begin{bmatrix} \rho\hat{U}_i \\ \rho u\hat{U}_i + \xi_{i_x} p \\ \rho v\hat{U}_i + \xi_{i_y} p \\ \rho w\hat{U}_i + \xi_{i_z} p \\ (\rho E + p)\hat{U} - \xi_{i_t} p \end{bmatrix} \quad (11)$$

Additionally the determinant of Jakobian J of the Cartesian coordinates $\vec{\xi} = (\xi, \eta, \zeta)^T$ of the equidistant mesh is introduced:

$$J = \begin{vmatrix} x_\xi & y_\xi & z_\xi \\ x_\eta & y_\eta & z_\eta \\ x_\zeta & y_\zeta & z_\zeta \end{vmatrix} \quad (12)$$

For a more detailed discussion on the coordinate transformation, in particular for moving meshes, see Visbal and Gaitonde [14]. With the Navier-Stokes equations in the finite-difference form, the ansatz of the Pade scheme can be utilized. The general equation for the approximation of a first difference of a function ϕ of 2^{nd} to 6^{th} order according to Lele [7] is:

$$\sum_{i=-1}^{1} \alpha_i \phi_i^{(1)} = \sum_{i=1}^{3} \frac{c_i}{2ih}(\phi_{+i} - \phi - i) \quad (13)$$

with i being an index, α_i the coefficients for the derivatives, c_i the coefficients for the original cell values, and h the cell spacing. Thus, the Pade scheme poses a line-implicit tri-diagonal system of equations, which can be efficiently solved by the Thomas algorithm. To numerically stabilize the scheme, the Pade filter is postulated as:

$$\alpha_f \tilde{\phi}_{i+1} + \tilde{\phi}_i + \alpha_f \tilde{\phi}_{i-1} = \sum_{n=0}^{N} \frac{a_n}{2}(\phi_{i+1} - \phi_{i-1}) \quad (14)$$

level	equivalent time step	initial revolutions	consequetive revolutions per trim iteration
coarse	2.00^o		
medium	0.50^o	4	2
fine	0.25^o		

Table 3: *Temporal settings assoziated with the different resolutions.*

with $\tilde{\phi}$ being the filtered function value, n the index distance from the current cell i and N being the total width of the filter. α_f is the filter constant, which analogous to $k^{(2)}$ and $k^{(4)}$ for the JST scheme allows to control the amount of filtering. It may be chosen between $-\frac{1}{2}$ and $\frac{1}{2}$. $\alpha_f = -\frac{1}{2}$ is the most dissipative setting and $\frac{1}{2}$ the least. In this work, α_f is chosen to be 0.499 and $N = 3$, which corresponds to a 6^{th} order filtering. The system of equations for the linear filter is also tri-diagonal and is solved the same way as the Pade scheme. To keep the accuracy within in the physical domain at 4^{th} order, four dummy layers are added to each block boundary for the data exchange between blocks, while it is only two dummy layers for the JST scheme.

The scheme is implemented as a cell-centered version into FLOWer by Enk [15]. The adaptation of the Chimera scheme is done according to Sherer and Scott [16], who end the implicit line at the beginning of a hole and restart the line after the hole as a new line through the adjustment of the coefficients.

2.5 Scheme Comparison

The major differences of the JST and Pade scheme are highlighted in the Table 4. Essentially, the JST scheme is a very robust scheme, which is able to compute a lot of different flow cases. However, the robustness comes at the price of increased numerical damping. Especially the modelling of the tip vortices becomes difficult with this scheme, as a high spatial (and temporal) resolution is necessary. The Pade scheme, through its higher order and low dissipative filtering proves to be very valuable for this task. However, with the necessary grid transformation and the inability to directly treat discontinuities such as shock waves, it is less suited for the blade grids. The grid quality requirements are a lot stricter for the Pade scheme than for the JST scheme. A negative determinant is more easily generated than a negative volume!

3 RESULTS

The comparative papers from van der Wall et al. [17] and Smith et al. [2] both present the blade mo-

scheme	JST	Pade
formulation	integral, finite-volume	transformed finite difference
solution type	explicit	line-implicit, tri-diagonal
metric	cell centered	
max formal order	2^{nd}	4^{th}
min formal order	1^{st}	4^{th}
filtering	2^{nd} and 4^{th}	6^{th}, (4^{th}, 8^{th})
shock-capturing	yes, through pressure sensor	no
low-pass filtering	4^{th} order	6^{th} order
recommended application	near wall meshes (due to grid quality), high gradient flows (shocks)	(farfield) vorticity transport, subsonic turbulent flows, (DNS/LES)

Table 4: *Comparison of the major attributes of the JST and Pade scheme as implemented in the FLOWer code*

tion plots with a subtracted mean, which is also true for the airloads plots. The airloads are presented by the Mach number scaled normal force coefficient $c_n M^2$ at the location 87% blade radius. For consistency, this is also done in this paper. The results section is divided into three sections. First the best way of modelling the blade motion is investigated, then the effect of the spatial and temporal resolution and finally alternative simulation techniques. For the first two sections, the viscous RANS simulation including the fuselage is utilized, while in the last section, the alternative approaches are reviewed along with the simulation including the fuselage.

3.1 Prescribed versus computed motion

As a first test, the synthesized blade motion found in the report by van der Wall [18] is prescribed in the CFD simulation. The four blades moved differently in the wind tunnel, which is then also modelled in the simulation. This simulation is analyzed in contrast with the solution of the fluid-structure coupling obtained from the HOST-FLOWer trim procedure. The emphasis is laid upon the reproduction of the airloads, which become important at the later step of the aeroacoustic prediction. As the correct trim procedure is mostly dependent on low-harmonic loads, the mid-level fuselage setup with the Hybrid scheme is utilized. Lim and Dimanlig [19] highlight that the effect of the fuselage is not negligible when trying to obtain a valid trim solution, while the rotor hub only plays a minor role. Therefore, the fuselage is included in this viscous simulation.

pitch angle	$\theta_0[^o]$	$\theta_c[^o]$	$\theta_s[^o]$
experiment	3.80	1.92	-1.34
simulation	3.72	1.87	-0.98
difference	0.08	0.05	-0.36

Table 5: *Trim angles of experiment and simulation*

Starting with the pitch control angles by the coupled simulation, their values are given Table 5 along with the experimental values. The collective pitch angle θ_0 and the lateral cyclic control angle θ_c align well with the experiment. Opposing this, the longitudinal cyclic control angle θ_s does not. In reference with the literature, these results are consistent with the ones obtained by Lim and Dimanlig [19], who arrive approximately at the same trim angles for their fluid-structure coupled model. Their collective and lateral cyclic angles are reduced, while their longitudinal angle matches better with the experiment.

Moving onto the blade tip motions, in Figure 5, the elastic deformations of the simulation and the experiment are graphed together. As the current version of the HOST-FLOWer coupling only rotors with identical blades can be modeled, the averaged prescribed motion and airloads are examined with the outcome of the fluid-structure coupling along with the error bars. In the plots, the mean is removed and listed in Table 6. The lead/lag deformation matches well on an integral level. The computed deformation is within the boundaries of the individual blades; however, the mean value deviates noticeably. The flapping motion shows little agreement between the experimental and the simulated results. The upward flapping on the retreating side is captured, while the advancing side of the simulation is offset from the experiment. Overall, the amplitude of the blade flapping of the simulation is too small in contrast to the experiment, which is also reflected by the absolute value of the mean. Last but not least, the tip torsion is investigated. Here, the simulation and experiment are more consistent. Yet, linked with the blade flapping the advancing side of the simulation, the computed blade torsion has a different behavior than the experiment. Except for this fact, the amplitude of the simulated torsion matches well with the one of the experiment. It is noted though that the mean value varies by 0.64^o, a non-negligible fact. The difference of the control angles is also associated with the differently resolved blade torsion, which

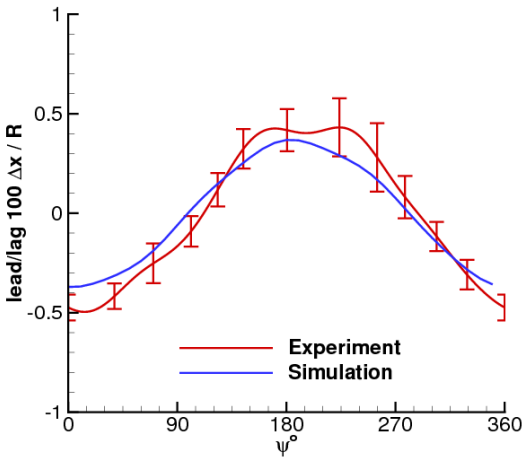

(a) Lead/Lag

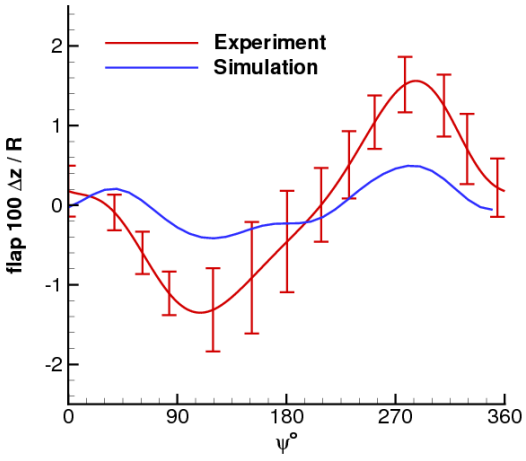

(b) Flapping

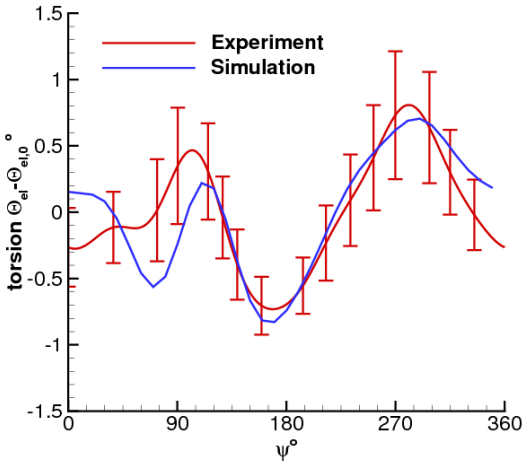

(c) Torsion

Figure 5: *Comparison of the elastic deformation at the blade tip of the experiment with the fluid-structure coupled results. Mean removed, the error bars mark the min/max from all blades.*

deformation	experiment	simulation	difference
lead/lag $100\Delta x/R$	1.40	2.91	-1.51
flap $100\Delta z/R$	-1.33	0.10	-1.43
torsion ^{o}	-1.09	-1.73	+0.64

Table 6: *Mean elastic deformation at blade tip*

in particular on the advancing side lead to different results.

Relating these results with the ones from the comprehensive code assessment of van der Wall et al. [17], where results with the HOST code using the free-wake module MESIR are presented, comparable offsets from the experiment are observed. The mean elastic blade tip torsion is under predicted and the mean blade flapping is too little in contrast with the experiment. Likely, the blade elastic model or the model of the fictive hinges requires improvement to arrive at a better agreement with the experiment.

The airloads of this case are presented in Figure 6. In the experiment, only the first blade is instrumented with pressure sensors. Thus, for the prescribed motion case, only the results of the first blade are presented. As with the blade motion, the mean is removed for clarity and listed in Table 7. It is seen that from $\psi \approx 270^o..70^o$ the amplitude of the prescribed motion airloads under predict the experiment, while from $\psi \approx 90^o..150^o$ an over prediction is observed. For the computed motion airloads, this deviation is reduced, and in particular the overshoot at $\psi \approx 100^o$ is reduced, though still given. The outcome of the prescribed motion is surprising as it is expected to at least reproduce the low-frequency content of the experimental airloads. A vague guess is made as to say that a static wind tunnel correction of 0.8^o for the shaft angle is insufficient and the wind tunnel itself should be modeled. The trimmed solution partially corrects this error as to match the resulting thrust, roll and pitching moment. This again, leads to the improved agreement of the airloads, which are part of the thrust integral. Checking the final thrust and power of the simulations, it is observed that the trim procedure managed to meet the experimental thrust, while the prescribed motion case largely over predicts this along with the required rotor power. Looking at the result by Tanabe and Sugawara [5], who apply the experimental blade deformation but seek the trim control angles independently of the experiment, they find a strong reduction of the collective pitch angle. This would indeed decrease the otherwise strongly over predicted thrust and also power.

It is decided to continue this study with the trimmed results, despite the minor discrepancies in the blade motion. Reason for this is the good alignment with the experimental trim control angles as well as the better correlation of the airloads, latter being the dominant factor for the aero-acoustic prediction.

	$c_n M^2$	thrust N	req. power kW
experiment	0.0902	3300	18.3
prescribed	0.11	3825	25.5
computed	0.0778	3304	22.0

Table 7: *Mean airloads of different motion approaches*

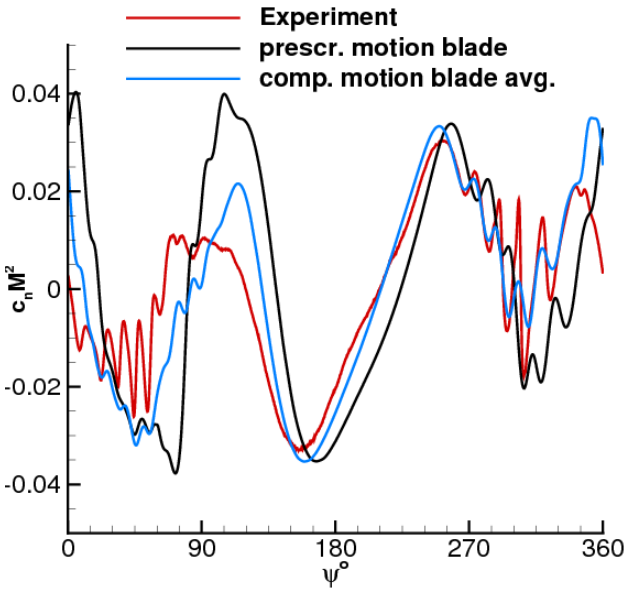

Figure 6: *Comparison of airloads between experiment and the simulation with prescribed and computed motion at $r/R = 87\%$.*

3.2 Grid Sensitivity Study

A grid sensitivity study is performed, where the effect of grid coarsening and refinement is analyzed with respect to the two simulation strategies. All three levels of refinement are trimmed solutions with a restriction concerning the simulation on the finest grids. The trim solutions from the medium level are recycled to initialize the flow field and then one full coupling step is performed afterwards. This is acceptable as the changes are relatively small between the medium and fine mesh when looking at Table 8. Here the control angles of the various refinement levels and simulation techniques are listed along with the experimental values. For both simulations, JST and Hybrid, it is observed that the collective pitch angles θ_0 decreases with increasing grid density, while the cyclic pitch angles θ_c and θ_s vary without a clear pattern. These variations are about an order of magnitude smaller than the reduction of the collective pitch angle and therefore considered to be of minor influence.

Moving onto the corresponding airload plots in Figure 7 and Figure 8 for the JST- and Hybrid simulations

pitch angle	$\theta_0[^o]$	$\theta_c[^o]$	$\theta_s[^o]$
experiment	3.80	1.92	-1.34
coarse (JST)	3.85	1.81	-1.02
medium (JST)	3.73	1.87	-0.96
fine (JST)	3.63	1.90	-1.03
coarse (Hybrid)	3.87	1.88	-1.07
medium (Hybrid)	3.72	1.86	-0.98
fine (Hybrid)	3.63	1.87	-0.99

Table 8: *Trim angles at different grid densities and schemes*

respectively, it is observed that the low-frequency content of the airloads is already well captured by the coarse level simulations, also supported by the good correlation of the mean airloads listed in Table 9. Yet, the prediction of required power is still significantly off for the coarse mesh setups. The full high-frequency content only becomes available on the finest grid levels and the computed required power approaches the experimental value. The major difference between the JST and Hybrid scheme is that the amplitude of these frequencies are greatly enlarged for the Hybrid scheme. The amplitudes on the advancing side at $\psi \approx 45^o...90^o$ is even over predicted by the Hybrid scheme on the medium and fine mesh being clearly visible in the derivative plot. The amplitudes on the retreating side at $\psi \approx 285^o...315^o$ are not fully recovered by either JST or Hybrid scheme, but the Hybrid scheme comes closer to the experiment than the JST scheme.

	$c_n M^2$	req. power kW
experiment	0.0902	18.3
coarse (JST)	0.0762	31.4
medium (JST)	0.0795	22.0
fine (JST)	0.0779	21.3
coarse (Hybrid)	0.0762	31.5
medium (Hybrid)	0.0778	22.0
fine (Hybrid)	0.0789	21.4

Table 9: *Mean airloads at different grid densities and schemes*

The greater capturing of the amplitudes and the high-frequency content through the Pade scheme is grasped on a qualitative level, when looking at the vorticity plots of the two schemes on the finest mesh, Figure 9. The Hybrid simulation not only resolves a lot more flow features, also the vortex strength is kept longer, while the vortex cores are sharper in contrast to the JST simulation. An example of this can be found in the downwash of the wake, where only the first trailing vortex shows the strong red for its vorticity, while this is still given two revolutions later for the Hybrid scheme.

As the goal of this simulation is to generate feasible

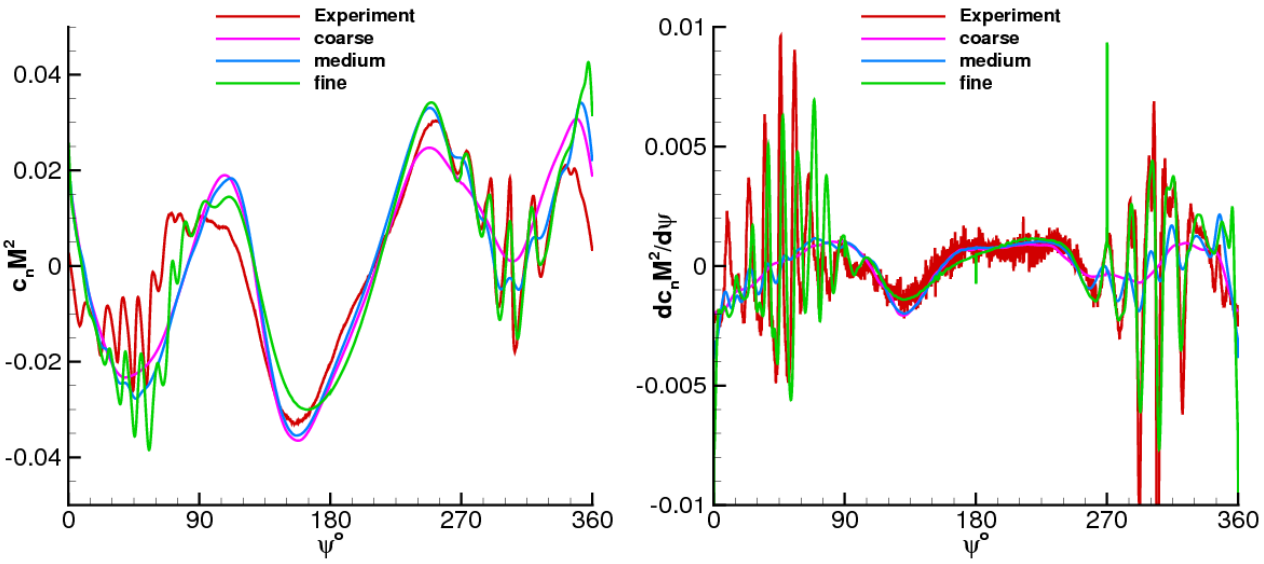

(a) airloads

(b) derivative of airloads

Figure 7: *Comparison of airloads between experiment and different grid sizes for the JST simulation at* $r/R = 87\%$.

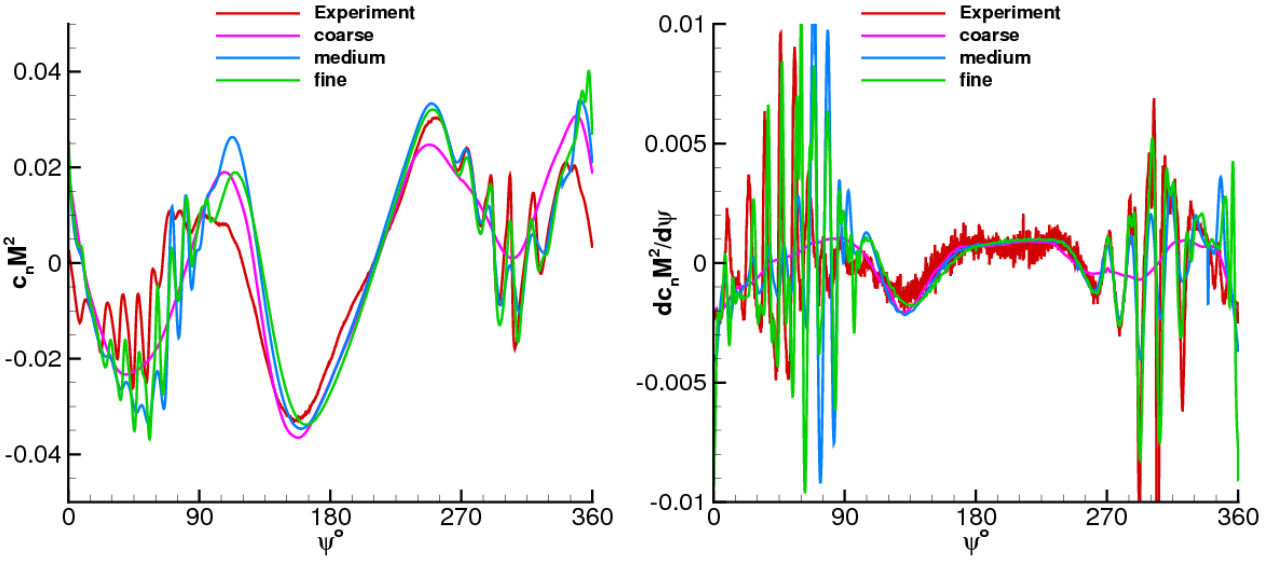

(a) airloads

(b) derivative of airloads

Figure 8: *Comparison of airloads between experiment and different grid sizes for the Hybrid simulation at* $r/R = 87\%$.

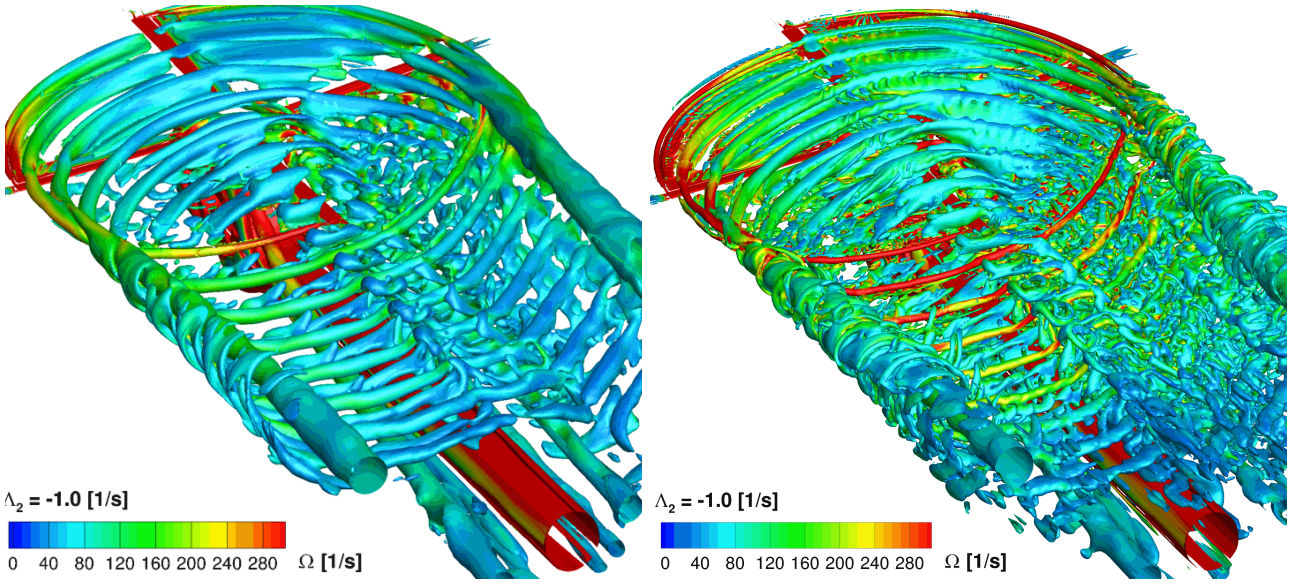

(a) JST (b) Hybrid

Figure 9: *Vorticity plots of the fine mesh simulations.*

data for the aero-acoustic simulation, the noise carpet plots of the experiment (Figure 10) and the simulations (Figure 11) are presented. On the coarsest grid level, the directivity and amplitude of the mid-frequency spectrum are not captured at all. Reason for this is that the vortex generation and conservation in the simulation is insufficient and only thickness and classical loading noise is observed. The high-frequency BVI noise cannot be represented as the load alternation from the vortices are already not captured in the airloads. On the medium mesh, the advantage of using the Hybrid scheme is seen and a difference of about $6dB$ is found between the peaks of the JST and Hybrid scheme. As for the directivity, it is also better captured by the Hybrid scheme resolving the two BVI hot spots. However, the hot spot on the retreating side is somewhat misrepresented as it splits into two single peaks in the highly elevated region. Looking at the finest grid simulations, the JST scheme also resolves the retreating side as a double peak at this level, which leads to the conclusion that this peak is likely occurring from the lack of the fuselage in the acoustic simulation as its shielding and scattering effects are neglected. This and the not exactly matching blade motion are the reasons, why the Hybrid scheme even over predicts the noise levels on the finest mesh setup.

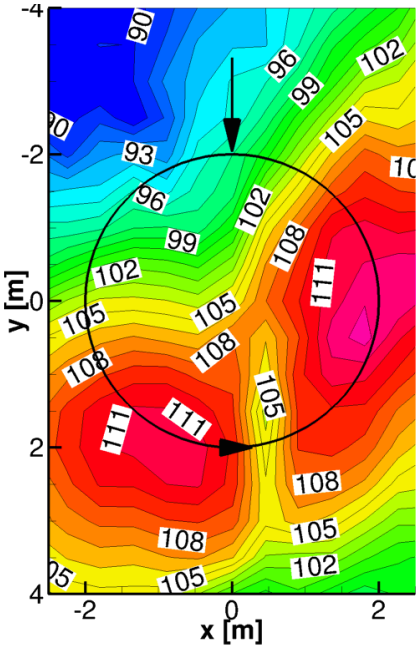

Figure 10: *Noise carpet of the HART II baseline experiment. SPL at 6-40 BPF plotted.*

As an estimator for the efficiency of the Hybrid scheme approach, the computational costs for one revolution are listed in Table 10. On the coarsest mesh, the Hybrid scheme even outperforms the JST scheme. Due to its tri-diagonal matrix, the solution is even quicker and the convergence rate is almost identical between the JST and Hybrid scheme. The advantage is lost on the finer grid levels as the blocking of the grid becomes make the implicit Pade scheme more and more inefficient. The stencil of the Pade scheme treats four cells at the boundary while in the field only two cells are treated; the filter even requires five cells at the boundary. In order to maintain the order, four dummy layers are required in contrast to two for the

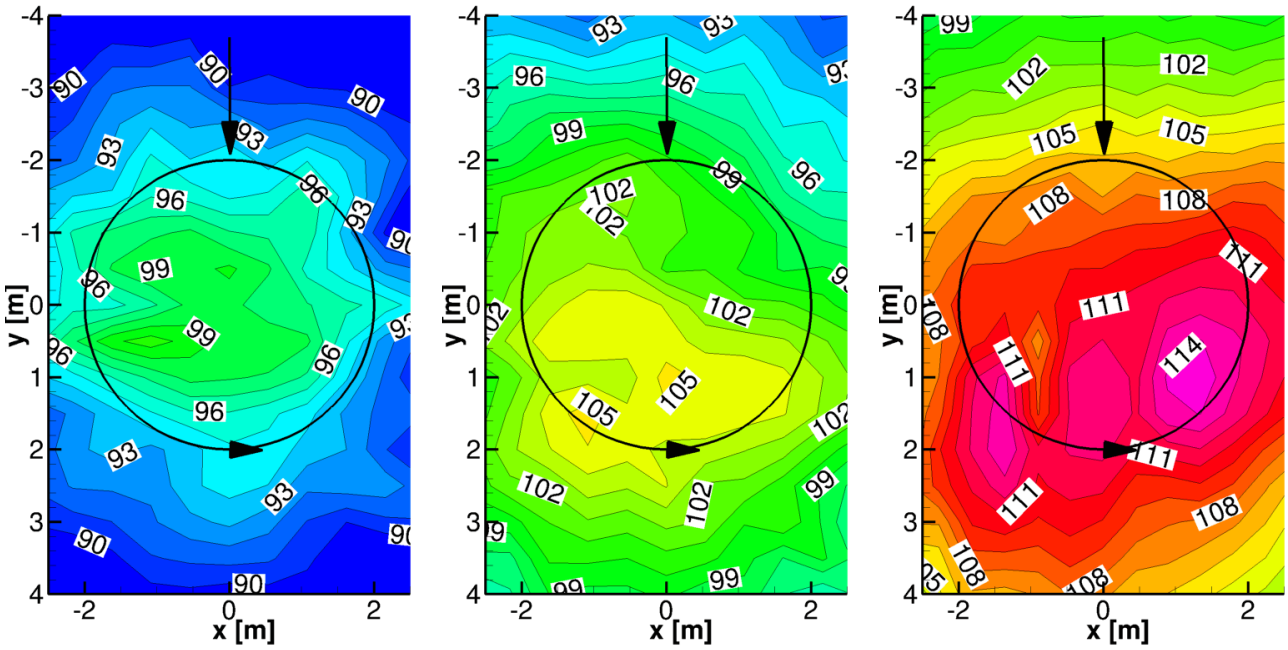

(a) JST - coarse (b) JST - medium (c) JST - fine

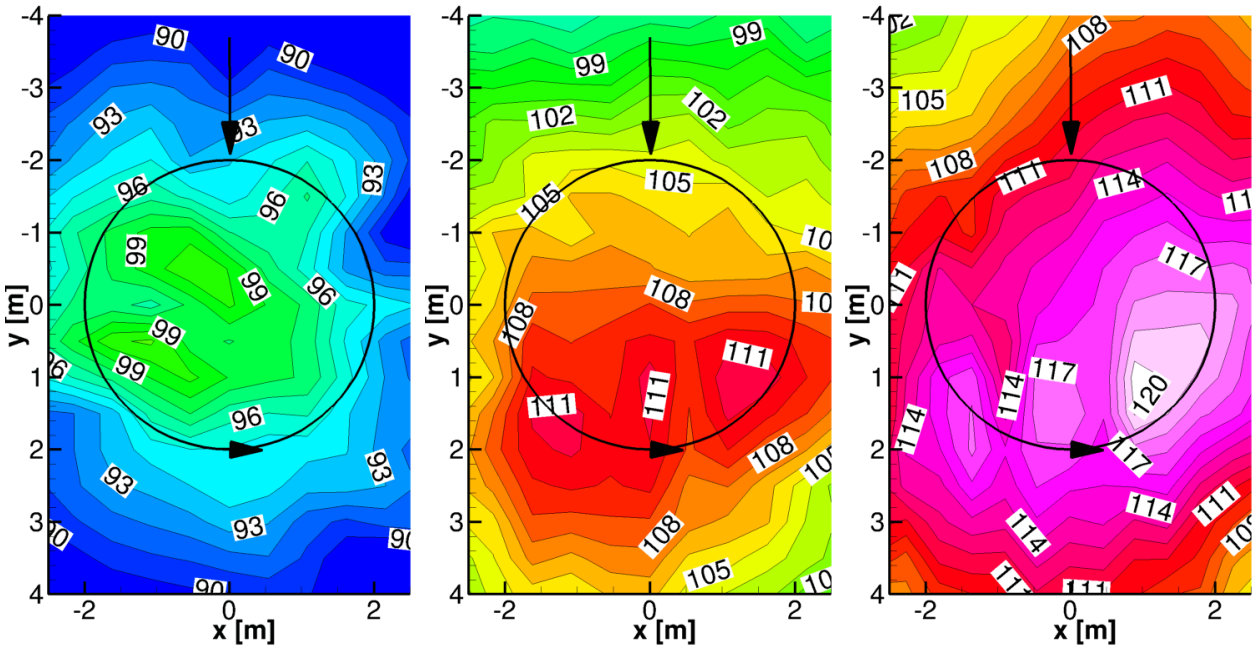

(d) Hybrid - coarse (e) Hybrid - medium (f) Hybrid - fine

Figure 11: *Comparison of noise carpets for the different simulation strategies. SPL at 6-40 BPF plotted.*

JST scheme, additionally increasing the resource demand and communication overhead. The finest mesh is highly blocked and therefore features a lot of block boundaries, thus more overhead is added slowing down the simulation. While the blocking is done manually and does not follow a strict rule, it is evident that with growing number of cells and grid blocks, the implicit Pade scheme becomes more expensive.

scheme/level	coarse	medium	fine
cores	24	72	384
blocks	84	174	500
JST (cpuh)	72	2,100	39,000
Hybrid (cpuh)	66	2,900	59,000
ratio	0.92	1.38	1.51

Table 10: *Computational cost for one rotor revolution for different schemes and resolutions.*

3.3 Alternative Simulation Techniques

So far, the HART II rotor has been simulated including the fuselage and viscosity. In this section, computational less demanding techniques are investigated. The simulations containing the fuselage are compared against isolated rotor simulations, an inviscid and a viscous simulation on the medium mesh setup. The Hybrid scheme is used throughout this section. Looking at the control angles in Table 11, it is seen that the inviscid simulation lowers the collective pitch angles θ_0, while the viscous isolated rotor simulation raises it in contrast to the viscous simulation where the fuselage is included. They all remain below the experiment though. The cyclic pitch angle θ_c is similar between the isolated rotor simulations and reduced in contrast to the fuselage simulation. This observation has already been made by Lim and Dimanlig [19], who examine the effect of including hub and fuselage in the simulation. The lateral cyclic pitch angle θ_s seems to behave differently. For the inviscid simulation it is close to the viscous simulation including the fuselage, while the viscous isolated rotor simulation has a larger offset.

pitch angle	$\theta_0[^o]$	$\theta_c[^o]$	$\theta_s[^o]$
experiment	3.80	1.92	-1.34
isolated inviscid	3.60	1.68	-1.03
isolated viscous	3.77	1.63	-0.85
+ fuselage viscous	3.72	1.86	-0.98

Table 11: *Trim angles of different simulation strategies*

Continuing with the airloads, the mean $c_n M^2$ correlates closely with the collective pitch angle θ_0, Table 12, while the computed power does not. The inviscid simulation strongly under predicts the required power simply due to the lack of viscosity in the simulation. Still, this result is feasible when checking against the results of the momentum theory of $2.32kW$, which assumes uniform inflow. The simulation with the fuselage consumes more power than the isolated rotor simulation as the blocking effect of the fuselage requires more power to maintain the same thrust.

	$c_n M^2$	req. power kW
experiment	0.0902	18.3
isolated inviscid	0.0765	4.83
isolated viscous	0.0789	21.1
+ fuselage viscous	0.0778	22.0

Table 12: *Mean airloads on medium mesh of different simulation strategies*

Analysing the airloads plots in Figure 12, it is observed that neglecting the fuselage leads to a phase-shift in the airloads. The low point of the airloads at $\psi \approx 150^o$ is shifted to $\psi \approx 180^o$ for the isolated viscous simulation. The steepness of this belly is also different among the methods with the inviscid one having the roundest shape. Looking at the derivative of the airloads, the high-frequency peaks are also phase shifted for the isolated rotor simulations in contrast with the simulation where the fuselage is included and the experiment. The amplitude of the peaks is also reduced with the inviscid simulation having the smallest ones.

Moving onto the noise carpets displayed in Figure 13, the inviscid simulation shows the so far best agreement with the experiment. This is due to the cancelation of errors. The lack of the fuselage in the aerodynamic and acoustic simulation as well as the changed trim solution overall balance themselves out. Still, the main driver remains the isolated rotor and directivity along with amplitude is well captured. Opposing this, the viscous simulation without the fuselage resolves the noise level appropriately, though it does not match the directivity of the experiment. Besides the two BVI noise peaks an artificial third peak is resolved on the advancing side of the blade, which is traced back to the already observed strong phase-shift in the airloads and elongated range of BVI on the advancing side.

The necessary resources for the alternative simulation strategies are listed in Table 13. Leaving the fuselage out of the simulation grants resource savings of about 24%, while going inviscid only brings an additional 13%. Relatively between the inviscid and viscous simulation without fuselage, another 15% in speed-up is observed. The strongest driver for the simulation costs are the grid points and the greatest amount of them is spent on the background mesh, thus inserting the points for the boundary layer in the blade

meshes has a minor impact on the computation time.

simulation	cpu time	ratio
isolated inviscid	1,800	0.63
isolated viscous	2,200	0.76
+ fuselage viscous	2,900	1.00

Table 13: *Computational cost for one rotor revolution for different simulation strategies.*

4 CONCLUSIONS

This paper reviewed an efficient technique for the resolution of BVI noise in CFD simulations. The implicit compact Pade scheme of 4^{th} order has good vortex conservation properties and has therefore been tested for the simulation of the HART II baseline test case. It is applied to convect the vortices in the background mesh, while the rotor blades are still modelled with the JST scheme, referring to this method as Hybrid scheme. With this Hybrid scheme, three tests were performed:

1. A study has been undertaken investigating the effect of different motion modelling using either the recorded motion from the experiment to be prescribed in the CFD simulation or the motions obtained by a fluid-structure coupled process. It is seen that neither the prescribed blade motion nor the computed one can exactly replicate the experimental results. Possible reasons for this are:

   (a) The simulated motion may contain errors in the structural modelling. In the comparative paper by Smith et al. [2], an offset in the blade modes is observed when the HOST code is utilized. Improving the structural model may yield a better correlation of the torsional motion, which is the most significant one for the airloads.

   (b) The prescribed motion with the given control angles from the experiment may feature errors. Indicators for this are on the one hand the here shown results, on the other hand Tanabe and Sugawara [5] are also unable to obtain exactly matching results and re-trim the control angles to improve their results.

   (c) The wind tunnel correction of 0.8^o assumes that the inflow deflection in the rotor plane is constant throughout the rotor plane. Increasing the detail and complexity of the simulation by inserting the inflow nozzle and the support sting as well as the well floor and ceiling of the open test section may allow for better matching inflow conditions.

   The best match of the airloads has been achieved with the fluid-structure coupled motion and is utilized for the following tests.

2. A benchmark of the Hybrid-Scheme with the traditional JST scheme is performed on three grid levels. It becomes clear that utilizing the Pade scheme in the background mesh allows for a much better resolution of the vorticity field surrounding the rotor. This again allows for a much better representation of the aero-acoustics. The cost increase is about 51% on the finest mesh setup, which when compared to other higher-order approaches is in a good standing.

3. A search for alternative, more efficient aero-acoustic simulation techniques applying the Hybrid scheme is done by looking at isolated rotor simulations, either inviscid or viscous. For aero-acoustic design purposes, utilizing a mesh in the range of 12 million points with an inviscid simulation technique shows promising results. Due to the neglected physical friction, the vortex conservation is additionally increased, while skipping the fuselage in the simulation along with the boundary layer resolution further speeds up the simulation. If the required power is of importance, it is recommended to go with the viscous simulation.

Future research may include:

- The medium mesh simulation with the fuselage and the Hybrid scheme showed good results and resolved the airload peaks already better than the fine mesh simulation with the JST scheme. Two options may allow the medium mesh Hybrid simulation to already surpass the fine mesh JST simulation with decreased costs:

  1. Decreasing the time step to the fine mesh simulation may allow to resolve the same amount of high-frequency content
  2. Utilizing the finer blade meshes with the medium background mesh may also allow for more vorticity to be injected in the background mesh, thus to resolve the correct amount of BVI

- The acoustic simulation may be improved by either directly evaluating the acoustic carpet in the background mesh of the CFD simulation or at least inserting the fuselage through the porous formulation of the FW-H equations in the acoustic simulation. This should include scattering and shielding effects of the fuselage.

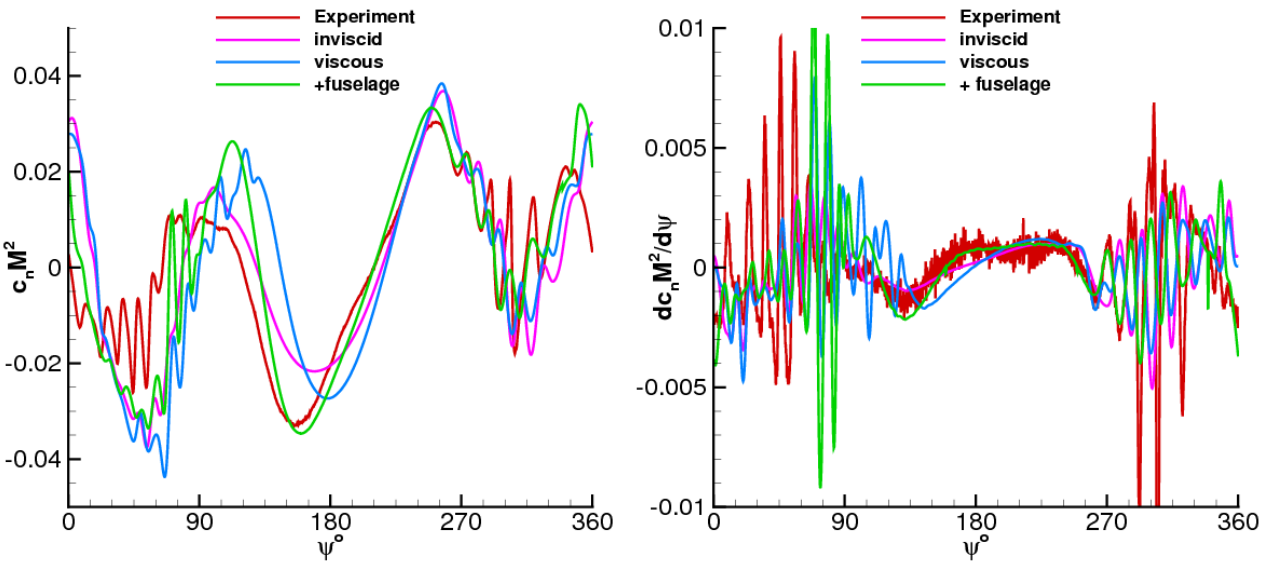

(a) airloads

(b) derivative of airloads

Figure 12: *Comparison of airloads between experiment and different simulation strategies at* $r/R = 87\%$.

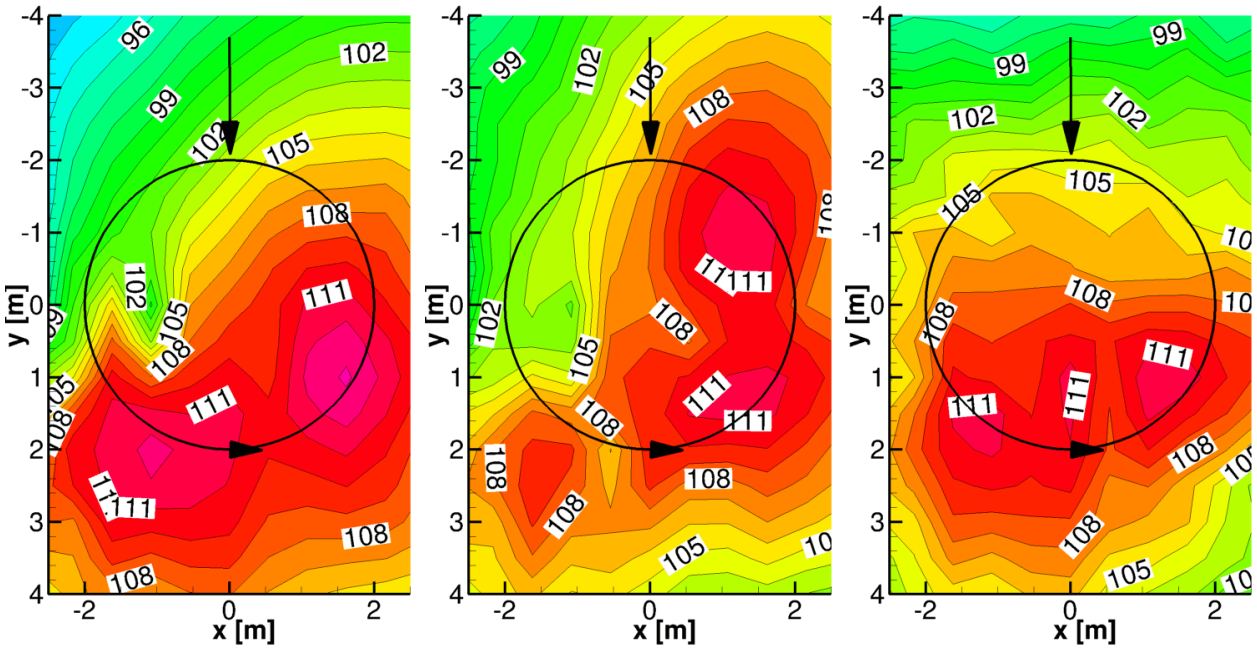

(a) inviscid

(b) viscous

(c) +fuselage

Figure 13: *Comparison of noise carpets with different simulation techniques. SPL at 6-40 BPF plotted.*

References

[1] B. G. van der Wall: A Comprehensive Rotary-Wing Data Base for Code Validation: The HART II International Workshop. In: *The Aeronautical Journal* 115 (2011), Nr. 1164, S. 91–102

[2] M. J. Smith, J. W. Lim, B. G. van der Wall, J. D. Baeder, R. T. Biedron, D. D. Boyd Jr, B. Jayaraman, S. N. Jung and B-Y Min: An assessment of CFD/CSD prediction state-of-the-art using the HART II international workshop data. In: *68th Annual Forum of the American Helicopter Society*, 2012

[3] J. W. Lim, A. Wissink, B. Jayaraman, and A. Dimanlig: Helios Adaptive Mesh Refinement for HART II Rotor Wake Simulations. In: *Annual Forum 68 of the American Helicopters Society*, 2012

[4] R. K. Jain, J. W. Lim, and B. Jayaraman: Modular Multisolver Approach for Efficient High-Fidelity Simulation of the HART II Rotor. In: *Journal of American Helicopter Society* (2015)

[5] Y. Tanabe and H. Sugawara: Construction and Validation of an Analysis Tool Chain for Rotorcraft Active Noise Reduction. In: *38th European Rotorcraft Forum*, 2012

[6] U. Kowarsch: Aeroacoustic Simulation of a Complete H145 Helicopter in Descent Flight. In: *41st European Rotorcraft Forum*, 2015

[7] Sanjiva K. Lele: Compact finite difference schemes with spectral-like resolution. In: *Journal of Computational Physics* 103 (1992), Nr. 1, 16 - 42. – ISSN 0021–9991

[8] A Jameson, W. Schmidt, and E. Turkel: Numerical Solution of the Euler Equations by Finite Volume Methods Using Runge-Kutta Time-Stepping Schemes. In: *AIAA, Fluid and Plasma Dynamics Conference, 14th*, 1981

[9] B. Benoit, A.-M. Dequin, K. Kampa, W. von Grünhagen, P.-M. Basset, and B. Gimonet: HOST, a General Helicopter Simulation Tool for Germany and France. In: *56th Annual Forum of the American Helicopters Society*, 2000

[10] J. Raddatz, and J. Fassbender: Block structured Navier-Stokes solver FLOWer. MEGAFLOW - Numerical Flow Simulation for Aircraft Design. In: *Notes on Numerical Fluid Mechanics and Multidisciplinary Design* 89 (2005), S. 27–44

[11] M. Dietz, W. Khier, B. Knutzen, S. Wagner, and E. Krämer: Numerical Simulation of a Full Helicopter Configuration Using Weak Fluid-Structure Coupling. In: *American Institute of Aeronautics and Astronautics*, 2007

[12] D. C. Wilcox ; La Canada, CA (Hrsg.): *Turbulence Modeling for CFD, 2nd ed.* DCW Industries, Inc, 1998

[13] C. B. Allen: CHIMERA volume grid generation within the EROS code. In: *Proceedings of the Institution of Mechanical Engineers, Part G: Journal of Aerospace Engineering* 214 (2000), 125-140

[14] M. R. Visbal and D. V. Gaitonde: On the Use of Higher-Order Finite-Difference Schemes on Curvilinear and Deforming Meshes. In: *Journal of Computational Physics* 181 (2002), Nr. 1, 155 - 185. – ISSN 0021–9991

[15] S. Enk: *Zellzentriertes Padeverfahren für DNS und LES*, Technische Universität Carolo-Wilhelmina Braunschweig, Dissertation, 2015

[16] S. E. Sherer and J. N. Scott: High-order compact finite-difference methods on general overset grids. In: *Journal of Computational Physics* 210 (2005), Nr. 2, 459 - 496. – ISSN 0021–9991

[17] B. G. van der Wall, S. N. Jung, J. W. Lim, M. J. Smith, J. Bailly, J. D. Baeder, and D. D. Boyd, Jr.: An Assessment of Comprehensive Code Prediction State-of-the-Art Using the HART II International Workshop Data. In: *Annual Forum 68 of the American Helicopters Society*, 2012

[18] B. G. van der Wall: Mode identification and data synthesis of HART II blade deflection data / Institute of Flight Systems, DLR Braunschweig. 2007. – Forschungsbericht

[19] J. W. Lim, and A. C. B. Dimanlig: The Effect of Fuselage and Rotor Hub on Blade-Vortex Interaction Airloads and Rotor Wakes. In: *36th European Rotorcraft Forum*, 2010